Curvature-Induced Cell Rearrangements in Biological Tissues

Yuting Lou, Jean-Francois Rupprecht, Sophie Theis, Tetsuya Hiraiwa, Timothy E Saunders

Curvature-induced cell rearrangements in biological tissues

Yuting Lou,[1,*] Sophie Theis,[2,†] Jean-Francois Rupprecht,[1,3,‡] Tetsuya Hiraiwa,[1,§] and Timothy E Saunders[1,2,¶]

[1] *Mechanobiology Institute, National University of Singapore*
[2] *Warwick Medical School, University of Warwick, Coventry, United Kingdom*
[3] *Aix Marseille Université, Université de Toulon, CNRS, Centre de Physique Théorique, Turing Center for Living Systems, Marseille, France*

On a curved surface, epithelial cells can adapt to geometric constraints by tilting and by exchanging their neighbors from apical to basal sides, known as an apicobasal T1 (AB-T1) transition. The relationship between cell tilt, AB-T1 transitions, and tissue curvature still lacks a unified understanding. Here, we propose a general framework for cell packing in curved environments and explain the formation of AB-T1 transitions under different conditions. We find that steep curvature gradients can lead to cell tilting and induce AB-T1 transitions. Conversely, large curvature anisotropy can drive AB-T1 transitions by hydrostatic pressure. The two mechanisms compete to determine the impact of tissue geometry and mechanics on optimized cell rearrangements in 3D.

As the external surfaces and barriers of many organs, epithelial tissues have to mechanically adapt to their environment [1, 2]. Extensive research into cell shape in 2D [3–10] and 3D [11–14] has revealed insights into how cells pack and undergo rearrangement during epithelial tissue formation [7–10, 15]. Cellular dynamic processes, like division and apoptosis, can rearrange cell neighbors. T1-transitions - the exchange of neighbors without altering the cell number - is another ubiquitous mechanism of cell rearrangements [16, 17]. T1 transitions are important in mediating planar tissue dynamics. For example, oriented T1 transitions can lead to tissue elongation or flow [15, 18–20], and the energetic barriers for T1 transitions to occur can dictate tissue fluidity/solidity [9, 21–23].

For a cell monolayer under 3D geometric constraint, cells can undergo apical-basal T1 (AB-T1) transitions (Fig. 1A, top). Different from the planar and dynamic T1-transitions described above, AB-T1 transitions are a static exchange of neighbors from the apical to basal layers of the cell. Such a 3D cellular arrangement, termed as a *scutoid* in the context of epithelial tissues [24–26] (Fig. 1A), has been observed in foams [27, 28] and biological systems with curved surfaces [29–33].

Tissue curvature is proposed to be pivotal in inducing AB-T1 transitions. In the ellipsoidal early *Drosophila* embryo, AB-T1 transitions appear most frequently around 20-50μm from the embryo head, a region with low curvature anisotropy but large tilt of cell lateral membranes [29] (Fig. 1A). During salivary gland formation in the *Drosophila* embryo, AB-T1 transitions occur at maximal curvature anisotropy [24]. Models have been proposed for cell packing in these specific cases [24, 29], but there is currently no consensus on how curvature induces AB-T1 transitions.

* mbilouy@nus.edu.sg
† Sophie.Theis@warwick.ac.uk
‡ jean-francois.rupprecht@univ-amu.fr
§ mbithi@nus.edu.sg
¶ Lead contact: timothy.saunders@warwick.ac.uk

Here, we provide a framework for describing curvature-induced cell deformation, which can be generalized to an array of geometries, and discuss the interplay between cell mechanics and tissue geometry in inducing AB-T1 transitions. We demonstrate that in 3D environments with steep curvature gradient, cells can tilt in order to pack efficiently. These tilted lateral membranes can exert tensions that contribute to in-plane stresses of opposite sign on the apical and basal plane stresses, thereby leading to AB-T1 transitions. Conversely, when hydrostatic pressure dominates, we find that AB-T1 transitions occur in regions with high curvature anisotropy. Overall, we find that the combination of tissue curvature, pressure, and lateral tensions determines the location of AB-T1 transition events.

Framework: We treat the epithelia as a material composed of two connected thin shells, representing the apical and basal surfaces of the tissue. Assuming the radius of curvature to be significantly larger than the cell size, we can use a continuum mechanics model based on membrane theory for elastic thin shells, neglecting bending stresses. Lateral membranes are included as part of the external load on the shell. Motivated by the *Drosophila* embryo, salivary gland and oocyte geometries, we focus on axisymmetric geometries, which have rotational symmetry about a polar axis (Fig. 1B). For any infinitesimal surface element dA on the 3D curved shell, it has a normal direction dA, and two tangential directions along the meridian $d\varphi$ and latitudinal radii $d\theta$ (Fig. 1B).

The in-plane stresses in the apical or basal layer are described as a stress tensor $\hat{\sigma}$ bearing two principal stresses $\sigma_{\varphi\varphi}$, $\sigma_{\theta\theta}$ and a shear stress component $\sigma_{\theta\varphi}$, with the basis $\hat{n} = (d\varphi, d\theta)^T$. This stress tensor $\hat{\sigma}$ can be decomposed into a hydrostatic part $\hat{\sigma}_{\rm stat} = \frac{1}{2}\mathrm{Tr}(\hat{\sigma})I$, corresponding to isotropic forces that induce local expansion or shrinkage of cell areas, and a deviatoric part $\hat{\sigma}_{\rm dev} = \hat{\sigma} - \hat{\sigma}_{\rm stat}$ corresponding to the anisotropic forces that induce shearing or anisotropic bulk compression/stretching (Fig. 1C).

The above stresses are balanced by the external loads from the lateral and apical/basal membrane generated by cell deformation or cellular active forces [34, 35]. For simplicity, we only consider axisymmetric external load,

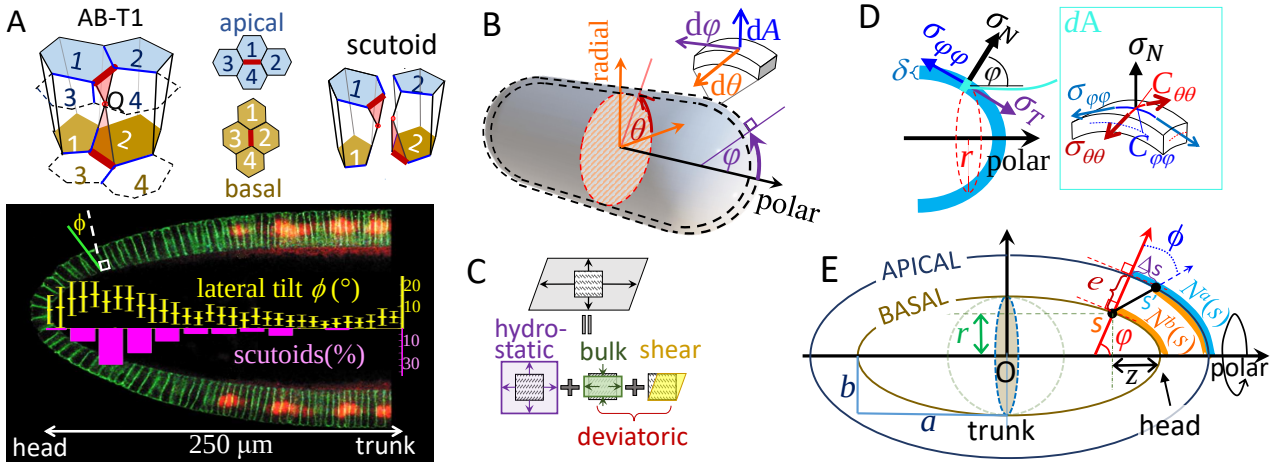

FIG. 1. The effect of curvature on cell packing and cellular forces. (A) Top: Scutoid geometry in epithelial tissues; point Q is the additional point shared by two columnar cells. The AB-T1 transition occurs at the edges highlighted in thick brown, leading to the exchange of neighbor pair from 1-4 (apical) to 2-3 (basal). Bottom: Tilt angle of lateral membrane (yellow) and percentage of scutoids (pink) peak near the head of a wild type *Drosophila* embryo, adapted from [29] under a Creative Commons License. (B) Two-layered model for curved epithelia on an axisymmetric object and the coordinates for a any local surface dA; (C) Graphical representation of the stress tensor decomposition, Eq. (1). (D) Force balance of a curved layer under axisymmetric loads: (left) at the meridional cut (red dashed ring) and (right) along the normal direction of the element surface $dA(\varphi,\theta)$. (E) A meridional cross section view of a two-layered prolate ellipse. The black tilted line is the tilted lateral membrane, with the basal end at s and the apical end at s', with the tilt angle ϕ and apical-basal distance e at s. The orange curves are the accumulated cell number from the head to s at the basal side; the skyblue curve is the accumulated cell number from the head to s at the apical side.

which can be decomposed into a normal part σ_N (positive pointing outward) and a tangential part along the meridian σ_T (positive pointing to the head) and hence the in-plane shear $\sigma_{\theta\varphi} \approx 0$. The meridional stress $\sigma_{\varphi\varphi}$ at any local cut (red ring in Fig. 1D) is balanced in the polar direction by the accumulated force over the revolved surface as:

$$\sigma_{\varphi\varphi} 2\pi r\delta \sin\varphi = \int_0^{s(\varphi)} \left[\sigma_N \cos\varphi + \sigma_T \sin\varphi\right] 2\pi r ds, \qquad (1)$$

where δ is the thickness of cell membrane, r is the distance to the polar axis from the local surface dA (Fig. 1D) and ds is the meridional arc length; See Supplemental Material (Supp. Mat.) at [] for the derivations of force balance. The circumferential stress $\sigma_{\theta\theta}$ is derived from force balance along the normal direction of the surface:

$$C_{\varphi\varphi}\sigma_{\varphi\varphi} + C_{\theta\theta}\sigma_{\theta\theta} = \frac{\sigma_N}{\delta}, \qquad (2)$$

where $C_{\varphi\varphi}$ and $C_{\theta\theta}$ are the principal curvatures along the meridional and circumferential direction, respectively.

AB-T1 transitions: The stresses in apical or basal layers can induce cell shape changes and cell intercalations. Here, we assume that prior to any applied external load, cells are relaxed to isotropic shapes without any deviatoric strain. AB-T1 transitions will take place most frequently when the apical and basal sides of a cell have oppositely directed deviatoric stresses [36] under external loading. In the absence of shear components $\sigma_{\varphi\theta}$, we can define a measure for AB-T1 transitions, γ, as proportional to the difference of the deviatoric strain between the apical and basal sides:

$$\gamma = \frac{\sigma^a_{\varphi\varphi} - \sigma^a_{\theta\theta}}{\mu_a} - \frac{\sigma^b_{\varphi\varphi} - \sigma^b_{\theta\theta}}{\mu_b}, \qquad (3)$$

where $\mu_{a,b}$ represent the effective elastic moduli at the apical and basal surfaces; $\gamma > 0$ corresponds to cells that are stretched along the meridional direction at the apical side while compressed along the circumferential direction at the basal side. The parameter-dependence of $\mu_{a,b}$ depends on the underlying material properties. Taking different forms for $\mu_{a,b}$ does not alter our key conclusions (See Supp. Mat. B for the results of different forms of μ). Here, we consider $\mu = |\mathrm{Tr}(\hat{\sigma})|$, which avoids introducing an intrinsic elastic modulus for the cells. Under typical physiological regimes for epithelial cells, we expect $|\mathrm{Tr}(\hat{\sigma}^{a,b})|$ to be non-zero, so γ behaves well.

We first consider the case when external loads are hydrostatic ($\sigma_T = 0$ and $\sigma_N = P$). With large curvature anisotropy, $|C_{\theta\theta} - C_{\varphi\varphi}|$, the magniture of γ is large, leading to AB-T1 transitions. In contrast, isotropic curvatures ($C_{\theta\theta} = C_{\varphi\varphi}$) lead to $\gamma = 0$ (Supp. Mat. C). This conclusion is consistent with the experimental observations in tubular epithelia [24].

Cell tilting: The results for hydrostatic systems above are not consistent with the AB-T1 transitions observed in the head of the early *Drosophila* embryo [29], where the curvature is nearly isotropic. However, in this

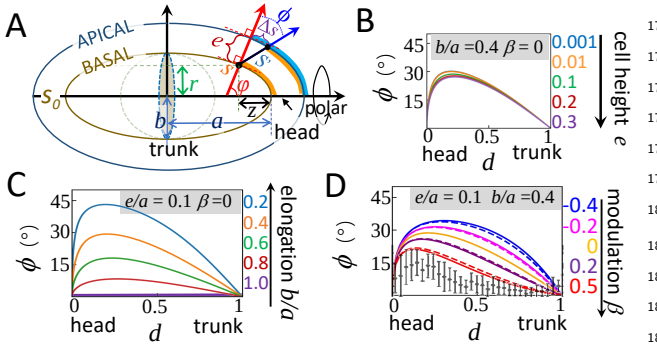

FIG. 2. The lateral tilt angle in the zero-lateral-tension limit, Eq. 6, as a function of the distance to the head along the polar direction $d = z/a$ (Fig. 1E) (A) under varying inverse aspect ratio b/a at $\varepsilon/a = 0.05, \beta = 0$; (B) under varying thickness modulation β at $\varepsilon/a = 0.01, b/a = 0.4$. Experimental data is shown for the cell tilt angle in the early *Drosophila* embryo ($b/a \sim 0.4, \beta \sim 0.5$), with s.d., by grey dots (data from [29]).

system, the cells are observed to tilt (Fig. 1A). The profile of external load σ_T, σ_N is affected by tilt of lateral membranes. We next investigated cell tilting within our model and explain its role in inducing AB-T1 transitions.

The tilted lateral membrane leans to the head by a small angle ϕ away from the normal direction (illustrated in Fig. 1E) as

$$\tan\phi(s) \sim \frac{\Delta s}{e(s)} \sim \frac{N^a(s) - N^b(s)}{2\pi r^a(s) e(s) \rho^a(s)}, \tag{4}$$

where Δs is the distance between the apical projection of s and the apical end of the tilted lateral membrane s'; $e(s)$ is the distance between the apical and basal layer; $\rho^{a,b}(s)$ is the cell density; $r^{a,b}(s)$ is the distance from s to the polar axis; $N^{a,b}(s) = \int_0^s \rho^{a,b} dA^{a,b}$ are the accumulated number of cells from the head apex to the coordinate s on the apical and basal sides, respectively. Although Fig. 1E is illustrated for an prolate ellipsoid, Eq. 4 works for any arbitrary axisymmetric shape.

The distribution of $\rho^{a,b}(s)$ and $e(s)$ are interdependent, as a consequence of minimizing the system free energy including the contributions from cell lateral membranes (See Supp. Mat. G). If the lateral membrane tensions are weak compared with the apical and basal cell layers, the apico-to-basal density ratio $\rho^a(s)/\rho^b(s)$ converges to a space-independent constant (Supp. Mat. D). In this limit, the tilt angle

$$\phi(s) = \phi^*(s)(1 - \tilde{k}), \tag{5}$$

where $\tilde{k} \ll 1$ is the ratio of tension strength between the lateral and apical/basal layers; ϕ^* is the tilt in the limit of zero lateral tension, depending on the curvature as:

$$\tan\phi^*(s) \sim \frac{N^b(s)(N_{\text{total}} - N^b(s)\left[\overline{H(s_1)} - \overline{H(s_2)}\right]}{\pi r^a(s)\rho^b(s)N_{\text{total}}}, \tag{6}$$

where $\overline{H(s_1)}$ and $\overline{H(s_2)}$ are the mean curvature weighted by cell numbers in a range of $0 < s_1 < s$ and $s < s_2 < s_0$, respectively (s_0 is the half meridian). For a convex object, a large gradient of $H(s)$ corresponds to a large magnitude of ϕ^* at s, with the corresponding tilt direction towards the region of higher positive curvature (See Supp. Mat. D for the derivations).

Conversely, if lateral membranes are extremely rigid, the lateral membrane tends to stand perpendicular to the surfaces, and $\rho^a(s)/\rho^b(s)$ equals inverse apico-to-basal area ratio $dA^b(s)/dA^a(s)$, hence the tilt vanishes (Supp. Mat. F). To further simply the model, we show that the effect of any cell density inhomogeneity on cell tilt is negligible if cell density changes along the surface more slowly than the curvature does (See Supp. Mat. E for the analysis). We henceforth set a homogeneous density $\rho^{a,b}(s) = \rho_0^{a,b}$.

Ellipsoid case: We now apply this formalism to a prolate ellipsoidal geometry as shown in Fig. 1E. It has a major half axis a and minor half axis b (see Supp. Mat. F for parameterization and the calculation of the curvature). Tissue height is determined mainly by the intrinsic cell volume control [37]. To leading order in the arc length s to the head, the height profile reads

$$e(s) \approx \varepsilon\left[1 + \beta\left(\frac{s}{s_{1/4}} - \frac{1}{2}\right)\right] \quad \text{for} \quad s \in [0, s_{1/4}], \tag{7}$$

where $s_{1/4}$ is the 1/4 perimeter of the meridian ellipse and ε is the average cell height across the surface and β is a coefficient modulating the surface height with $\beta = 0$ representing homogeneous cell height. As we assume cell size is much smaller than the radius of curvature, the average height of the tissue ε has negligible impact on the tilt profile (see Supp. Mat. E for the discussions).

We calculate the cell tilt angle ϕ^* in the zero-lateral-tension limit as a function of the relative distance to the head of a prolate ellipsoid, $d(s) = z(s)/a$, where $z(s)$ is the distance to the head along the polar direction; $d = 0$ corresponds to the head and $d = 1$ to the trunk. The tilt angle increases with elongation of the ellipsoid (smaller b/a), Fig. 2A. For a typical value observed experimentally in *Drosophila* ($b/a \sim 0.4$ [29]), the tilt angle peaks around 30°. The impact of height inhomogeneity on the tilt angle is shown by Fig. 2B: a large, positive β (tissue height larger at the trunk) makes the peak of the tilt angle profile more pronounced. The calculated tilt profile is consistent with the data observed in the early *Drosophila* embryo ($\beta \sim 0.5$), with the predicted magnitude of ϕ^* (red curve) slightly larger than the experimental measurements (black dots, from [29]) as expected by Eq. 5.

External loads along the tilted lateral membranes can qualitatively change the stress distribution. We show in Fig. 3A-B a comparison of the stress components $\sigma_{\varphi\varphi}$ and $\sigma_{\theta\theta}$ between a hydrostatic case: $\sigma_T^a = \sigma_T^b = 0$, $\sigma_N^a = -\sigma_N^b = T$ and a case with the external stresses T along

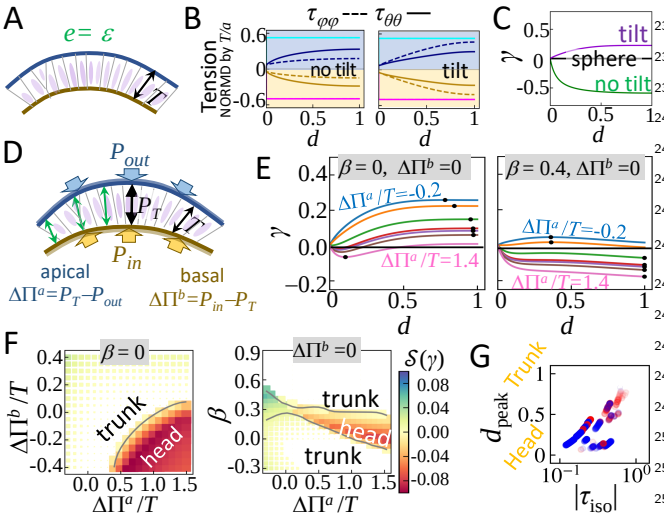

FIG. 3. AB-T1 transition rate γ calculated for a prolate ellipsoid with $b/a = 0.4$. (A) A schematic illustration of the system under tensile lateral stress T with a constant tissue height $\varepsilon = 0.05a$ for panel B and C; (B) In plane, apical and basal stress components normalized by Ta/δ as a function of the distance to the head. Left: T perpendicular to the layer (hydrostatic); right: T along tilted lateral membranes. The cyan and magenta curves stand for a sphere ($a = b$). The tensile stresses have a positive sign (apical,blue) and contractile stress has a negative sign (basal, yellow). (C) The correspondent AB-T1 rate γ for the prolate ellipsoid. (D) A schematic tissue setting under the external loads with pressures and inhomogeneous tissue height (Eq. 7). (E) Profile of the AB-T1 measure, γ, with varying apical pressure difference $\Delta\Pi^a$ and with basal pressure difference $\Delta\Pi^b = 0$. Left: the tissue height modulation rate $\beta = 0$; right: $\beta = 0.4$. Black dots indicate the peak, where the absolute AB-T1 measure $|\gamma|$ reaches the maximum. (F) The phase diagram for the peakiness of γ, which is calculated as $\mathrm{sign}(\gamma_{\mathrm{peak}}) \times ||\gamma_{\mathrm{peak}}| - |\gamma_{\mathrm{trunk}}||$. Left: $\beta = 0$; right: $\Delta\Pi^b = 0$. The size of the scattered square is $\propto (1 - d_{\mathrm{peak}})^2$, so positions closer to the head ($d = 0$) are represented by larger squares. The grey contours separate the trunk ($d_{\mathrm{peak}} > 0.5$) and the head ($d_{\mathrm{peak}} < 0.5$) regions.

tilted lateral membranes:

$$\sigma_T^a = T\sin\phi,\ \sigma_N^a = T\cos\phi,\ \sigma_T^b = -T\sin\phi,\ \sigma_N^b = -T\cos\phi.$$

The magnitude of $\sigma_{\theta\theta}$ and $\sigma_{\varphi\varphi}$ grows from the head to the trunk in different manners, depending on whether T is perpendicular to the shells (hydrostatic) or T along the tilted lateral membranes. The resultant AB-T1 transition rate, calculated through Eq. 3, flips its sign with or without the tilt (Fig. 3C). However, this qualitative difference will vanish when the surface approaches a sphere ($a/b = 1$) (Fig. 3B; cyan and magenta lines), leading to no AB-T1 transition at all locations (Fig. 3C; black line). 2 Next, we discuss results with pressure differences across the cell along the apical-basal axis (Fig. 3D). The tissue height follows Eq. 7. The apical and basal membranes are subject to pressure from: the outside P_{out}; from the internal cavity (*e.g.* yolk or luminal pressure) P_{in}; and inside the tissue P_T. The pressure differences at the apical and basal surfaces are given by $\Delta\Pi^a = P_T - P_{out}$ and $\Delta\Pi^b = P_{in} - P_T$ respectively, with positive $\Delta\Pi$ pointing towards the outside. Before applying external load, we assume cells have relaxed to their preferred cell shape with no internal strain. The external normal and tangential loads on the apical and basal side are $\sigma_N^{(a)} = \Delta\Pi + T\cos\phi$, $\sigma_T^{(a)} = \Delta\Pi + T\sin\phi$, $\sigma_N^{(b)} = \Delta\Pi + T\cos\phi$ and $\sigma_T^{(b)} = \Delta\Pi - T\sin\phi$.

The system dominated by pressure ($\Delta\Pi/T \to \infty$) corresponds to a hydrostatic limit, Fig. 3B (left). In this limit, the profiles of stresses and the consequent spatial distribution of AB-T1 transition frequency do not qualitatively depend on the pressure differences or the cell height profile (See Supp. Mat. C for the derivations). In contrast, strikingly, when the pressure difference is comparable with lateral stress ($\Delta\Pi \sim T$), γ is sensitive to the two pressure differences and β, Fig. 3E. $\Delta\Pi$ can be negative (pointing inwards), thus the normal component of lateral tension T can be partly balanced by this pressure and σ_T/σ_N becomes much larger as if the cells tilt more significantly. When $\Delta\Pi^a/T$ shifts sign from negative to positive, at the trunk ($d = 1$) γ becomes negative, altering the orientation of AB-T1 transitions.

To capture the key features of the distribution of γ, we define the peak of γ as where γ_{peak} is the maximal value of $|\gamma|$ (Fig. 3E) and its value at peak (referred here as the *peakiness*) as $\mathrm{sign}(\gamma_{\mathrm{peak}}) \times ||\gamma_{\mathrm{peak}}| - |\gamma_{\mathrm{trunk}}||$. Accordingly, we can construct a phase diagram of AB-T1 transitions, using the position of the peak and peakiness as the order parameters, Fig. 3F. We show the diagram in the $\Delta\Pi^a$-$\Delta\Pi^b$ space for $\beta = 0$ (left) and in the space of β-$\Delta\Pi^a/T$ with $\Delta\Pi^b = 0$ (right). The peak in the tendency of AB-T1 transition switches from trunk to head beyond a critical line $\beta(\Delta\Pi)$ (Fig. 3F). From these phase diagrams, we can estimate mechanical properties (*e.g.* pressure, lateral tension, or possible external loads) from the geometric cell profiles (*e.g.* cell tilt, cell height and AB-T1 locations/orientations).

Conclusions: We have proposed a model for the onset of cellular tilt within a curved monolayer. We find that the interplay between the lateral cell-cell tension and the cellular tilt leads to a shift in the location at which we expect the number of neighbor rearrangements to be maximal. Our formalism provides predictions for the location of AB-T1 transitions in several geometries that are echoed by experimental observations in various geometries [24, 29].

The lateral membranes play an essential role in balancing stress across the cell, thereby regulating cell shape. In particular, lateral membranes with low contractility lead to cell tilting, which cooperates with pressure and tissue thickness to result in a rich phase diagram for the tendency of AB-T1 transitions to occur. If the lateral membranes are sufficiently stiff, then the tilt of lateral membranes is suppressed and AB-T1 transitions occur at regions with large curvature anisotropy, following the model prediction in the hydrostatic limit.

Though we have focused on a prolate geometry with simple external loads, our formalism can be generalized to a diverse range of tissue geometries observed *in vivo*. We expect tilt to occur at the steepest curvature gradient, even for non-axisymmetric and non-closed surface geometries; *e.g.* the brain and gut. We can also explore the role of in-plane shear and bending within this theoretical framework. Internal cell strain, which is likely significant during cellular process such as cell division[38], can also be considered as a source of external loading. Finally, transient and reversible AB-T1 transitions have been observed [39, 40]; the dynamic aspect of AB-T1 transitions may be relevant to the mechanism of T1 transitions [23, 36] and their contributions to processes like tissue folding or buckling [41**?** –45] remains to be investigated.

We thank Jacques Prost for discussions leading to Eq. (4). J.-F.R. has received funding from France 2030, the French Government program managed by the French National Research Agency (ANR-16-CONV-0001) and from the Excellence Initiative of Aix-Marseille University - A*MIDEX and ANR-20-CE30-0023 grant. T.H. and T.E.S. are funded by Mechanobiology Institute seed grants. T.E.S. is also funded by start-up support from the University of Warwick.

[1] C. Guillot and T. Lecuit, Mechanics of epithelial tissue homeostasis and morphogenesis, Science **340**, 1185 (2013).

[2] E. Latorre, S. Kale, L. Casares, M. Gómez-González, M. Uroz, L. Valon, R. V. Nair, E. Garreta, N. Montserrat, A. Del Campo, *et al.*, Active superelasticity in three-dimensional epithelia of controlled shape, Nature **563**, 203 (2018).

[3] B. Aigouy, R. Farhadifar, D. B. Staple, A. Sagner, J.-C. Roper, F. Julicher, and S. Eaton, Cell flow reorients the axis of planar polarity in the wing epithelium of *drosophila*, Cell **142**, 773 (2010).

[4] A. Sagner, M. Merkel, B. Aigouy, J. Gaebel, M. Brankatschk, F. Jülicher, and S. Eaton, Establishment of global patterns of planar polarity during growth of the *drosophila* wing epithelium, Current Biology **22**, 1296 (2012).

[5] N. Khalilgharibi, J. Fouchard, N. Asadipour, R. Barrientos, M. Duda, A. Bonfanti, A. Yonis, A. Harris, P. Mosaffa, Y. Fujita, *et al.*, Stress relaxation in epithelial monolayers is controlled by the actomyosin cortex, Nature Physics **15**, 839 (2019).

[6] R. J. Tetley, M. F. Staddon, D. Heller, A. Hoppe, S. Banerjee, and Y. Mao, Tissue fluidity promotes epithelial wound healing, Nature Physics **15**, 1195 (2019).

[7] M. C. Gibson, A. B. Patel, R. Nagpal, and N. Perrimon, The emergence of geometric order in proliferating metazoan epithelia, Nature **442**, 1038 (2006).

[8] R. Farhadifar, J.-C. Röper, B. Aigouy, S. Eaton, and F. Jülicher, The influence of cell mechanics, cell-cell interactions, and proliferation on epithelial packing, Current Biology **17**, 2095 (2007).

[9] D. B. Staple, R. Farhadifar, J.-C. Röper, B. Aigouy, S. Eaton, and F. Jülicher, Mechanics and remodelling of cell packings in epithelia, The European Physical Journal E **33**, 117 (2010).

[10] L. Atia, D. Bi, Y. Sharma, J. A. Mitchel, B. Gweon, S. A Koehler, S. J. DeCamp, B. Lan, J. H. Kim, R. Hirsch, *et al.*, Geometric constraints during epithelial jamming, Nature Physics **14**, 613 (2018).

[11] X. Du, M. Osterfield, and S. Y. Shvartsman, Computational analysis of three-dimensional epithelial morphogenesis using vertex models, Physical Biology **11**, 066007 (2014).

[12] M. Krajnc and P. Ziherl, Theory of epithelial elasticity, Physical Review E **92**, 052713 (2015).

[13] A. G. Fletcher, F. Cooper, and R. E. Baker, Mechanocellular models of epithelial morphogenesis, Philosophical Transactions of the Royal Society B: Biological Sciences **372**, 20150519 (2017).

[14] M. Merkel and M. L. Manning, A geometrically controlled rigidity transition in a model for confluent 3d tissues, New Journal of Physics **20**, 022002 (2018).

[15] C. Bertet, L. Sulak, and T. Lecuit, Myosin-dependent junction remodelling controls planar cell intercalation and axis elongation, Nature **429**, 667 (2004).

[16] H. Honda, Y. Ogita, S. Higuchi, and K. Kani, Cell movements in a living mammalian tissue: Long-term observation of individual cells in wounded corneal endothelia of cats, Journal of Morphology **174**, 25 (1982).

[17] A. G. Fletcher, M. Osterfield, R. E. Baker, and S. Y. Shvartsman, Vertex models of epithelial morphogenesis, Biophysical Journal **106**, 2291 (2014).

[18] H. Honda, T. Nagai, and M. Tanemura, Two different mechanisms of planar cell intercalation leading to tissue elongation, Developmental Dynamics **237**, 1826 (2008).

[19] K. Sato, T. Hiraiwa, E. Maekawa, A. Isomura, T. Shibata, and E. Kuranaga, Left–right asymmetric cell intercalation drives directional collective cell movement in epithelial morphogenesis, Nature Communications **6**, 10074 (2015).

[20] T. Hiraiwa, E. Kuranaga, and T. Shibata, Wave propagation of junctional remodeling in collective cell movement of epithelial tissue: Numerical simulation study, Frontiers in Cell and Developmental Biology **5**, 66 (2017).

[21] D. Bi, J. Lopez, J. M. Schwarz, and M. L. Manning, A density-independent rigidity transition in biological tissues, Nature Physics **11**, 1074 (2015).

[22] D. Bi, X. Yang, M. C. Marchetti, and M. L. Manning, Motility-driven glass and jamming transitions in biological tissues, Physical Review X **6**, 021011 (2016).

[23] M. Krajnc, S. Dasgupta, P. Ziherl, and J. Prost, Fluidization of epithelial sheets by active cell rearrangements, Physical Review E **98**, 022409 (2018).

[24] P. Gómez-Gálvez, P. Vicente-Munuera, A. Tagua, C. Forja, A. M. Castro, M. Letrán, A. Valencia-Expósito, C. Grima, M. Bermúdez-Gallardo, Ó. Serrano-Pérez-Higueras, *et al.*, Scutoids are a geometrical solution to three-dimensional packing of epithelia, Nature Communications **9**, 1 (2018).

[25] G. Blanchard, A 3d cell shape that enables tube formation, Nature **561**, 182 (2018).

[26] P. Gómez-Gálvez, P. Vicente-Munuera, S. Anbari, J. Buceta, and L. M. Escudero, The complex three-dimensional organization of epithelial tissues, Development **148**, dev195669 (2021).

[27] E. B. Matzke, The three-dimensional shape of epidermal cells of the apical meristem of anacharis densa (elodea), American Journal of Botany **35**, 323 (1948).

[28] A. Mughal, S. Cox, D. Weaire, S. Burke, and S. Hutzler, Demonstration and interpretation of 'scutoid' cells formed in a quasi-2d soap froth, Philosophical Magazine Letters **98**, 358 (2018).

[29] J.-F. Rupprecht, K. H. Ong, J. Yin, A. Huang, H.-H.-Q. Dinh, A. P. Singh, S. Zhang, W. Yu, and T. E. Saunders, Geometric constraints alter cell arrangements within curved epithelial tissues, Molecular Biology of the Cell **28**, 3582 (2017).

[30] Y. E. Sanchez-Corrales, G. B. Blanchard, and K. Röper, Radially patterned cell behaviours during tube budding from an epithelium, Elife **7**, e35717 (2018).

[31] C. M. Nelson, Epithelial packing: even the best of friends must part, Current Biology **28**, R1197 (2018).

[32] K. Z. Perez-Vale and M. Peifer, Orchestrating morphogenesis: building the body plan by cell shape changes and movements, Development **147**, dev191049 (2020).

[33] C. Pérez-González *et al.*, Mechanical compartmentalization of the intestinal organoid enables crypt folding and collective cell migration, Nature Cell Biology **23**, 745 (2021).

[34] C. G. Vasquez and A. C. Martin, Force transmission in epithelial tissues, Developmental Dynamics **245**, 361 (2016).

[35] F.-L. Wen, Y.-C. Wang, and T. Shibata, Epithelial folding driven by apical or basal-lateral modulation: geometric features, mechanical inference, and boundary effects, Biophysical Journal **112**, 2683 (2017).

[36] C. Duclut, J. Paijmans, M. M. Inamdar, C. D. Modes, and F. Jülicher, Nonlinear rheology of cellular networks, Cells & Development **168**, 203746 (2021).

[37] L. Saias, J. Swoger, A. D'Angelo, P. Hayes, J. Colombelli, J. Sharpe, G. Salbreux, and J. Solon, Decrease in cell volume generates contractile forces driving dorsal closure, Developmental Cell **33**, 611 (2015).

[38] H. F. Gomez, M. S. Dumond, L. Hodel, R. Vetter, and D. Iber, 3d cell neighbour dynamics in growing pseudostratified epithelia, Elife **10**, e68135 (2021).

[39] A. C. Martin and B. Goldstein, Apical constriction: themes and variations on a cellular mechanism driving morphogenesis, Development **141**, 1987 (2014).

[40] Z. Sun, C. Amourda, M. Shagirov, Y. Hara, T. E. Saunders, and Y. Toyama, Basolateral protrusion and apical contraction cooperatively drive *drosophila* germ-band extension, Nature Cell Biology **19**, 375 (2017).

[41] E. Hannezo, J. Prost, and J.-F. Joanny, Instabilities of monolayered epithelia: shape and structure of villi and crypts, Physical Review Letters **107**, 078104 (2011).

[42] E. Hannezo, J. Prost, and J.-F. Joanny, Theory of epithelial sheet morphology in three dimensions, Proceedings of the National Academy of Sciences **111**, 27 (2014).

[43] S. Alt, P. Ganguly, and G. Salbreux, Vertex models: from cell mechanics to tissue morphogenesis, Philosophical Transactions of the Royal Society B: Biological Sciences **372**, 20150520 (2017).

[44] N. Harmand, A. Huang, and S. Hénon, 3d shape of epithelial cells on curved substrates, Physical Review X **11**, 031028 (2021).

[45] A. Trushko, I. Di Meglio, A. Merzouki, C. Blanch-Mercader, S. Abuhattum, J. Guck, K. Alessandri, P. Nassoy, K. Kruse, B. Chopard, *et al.*, Buckling of an epithelium growing under spherical confinement, Developmental Cell **54**, 655 (2020).